remote sensing

MDPI

Technical Note

Hail Event Detection Using Power Spectrum Characteristics of Coherent Doppler Lidar: A Case Study in Hefei

Kenan Wu [1,*], Yang Sun [2], Jiadong Hu [3], Tianwen Wei [3], Xiaodan Hu [1], Mengya Wang [3] and Haiyun Xia [2,3]

[1] School of Information Engineering, HuangShan University, Huangshan 245041, China; huxiaodan@hsu.edu.cn
[2] School of Earth and Space Sciences, University of Science and Technology of China, Hefei 230026, China; suny212@mail.ustc.edu.cn (Y.S.); hsia@ustc.edu.cn (H.X.)
[3] School of Atmospheric Physics, Nanjing University of Information Science and Technology, Nanjing 210044, China; hujd0707@nuist.edu.cn (J.H.); twwei@nuist.edu.cn (T.W.); wmengya123@nuist.edu.cn (M.W.)
* Correspondence: 600304@hsu.edu.cn

Highlights

What are the main findings?

- Hail and rainfall have distinct coherent Doppler lidar (CDL) power spectrum characteristics, with hail featuring higher vertical velocities, a wider spectrum width, and skewness with absolute values near 1.
- CDL can identify hail-dominated periods in mixed-phase precipitation under weak convective conditions.

What are the implications of the main findings?

- Hail's unique power spectrum characteristics can facilitate the practical development and implementation of CDL-based hail detection algorithms for complex precipitation conditions.
- The power spectrum discrimination method, assisted by the high spatiotemporal resolution of CDL, provides support for accurate short-term nowcasting prior to hail generation.

Abstract

Hail is one of the typical manifestations of severe convective weather, characterized by its sudden onset and strong localization. In this study, a compact all-fiber coherent Doppler lidar (CDL) working at the 1.5 μm wavelength is employed to detect a hail event. Combined with ERA5 reanalysis data, Parsivel^2, and cloud-type products from the Fengyun satellite, the synoptic background of the hail event was analyzed. Owing to its high-precision spectrum measurement capability, the CDL can effectively separate the multi-component power spectra of precipitation particles. By comparing particle velocity, spectrum width and skewness as characteristic parameters from signal separation across light rain, hail and heavy rain, the distinctive power spectrum characteristics of hail were identified. This study verifies that CDL can provide high-spatiotemporal-resolution data support for the short-term forecasting of hail events.

Keywords: lidar; hail; precipitation detection; power spectrum; multi-peak Gaussian fitting

Academic Editor: Weiqiang Ma

Received: 30 January 2026
Revised: 24 March 2026
Accepted: 1 April 2026
Published: 2 April 2026

1. Introduction

Hail is one of the typical outcomes of severe convective weather. Its formation and development are closely associated with intense vertical motions and the accumulation of unstable energy in the atmosphere, often accompanied by extreme meteorological phenomena such as thunderstorms and short-duration heavy precipitation [1]. Characterized by remarkable suddenness and locality, hail particles pose a severe threat to humans, animals, crops, and public infrastructure due to their large momentum and size [2–4]. In actual hail events, ground observations commonly record information including hail diameter, spatial coverage of hail, and the associated damage to crops and buildings [5]. Such events are often accompanied by frequent lightning activity, vigorous convective cloud development, intense short-duration rainfall, and abrupt increases in surface wind gusts [6,7]. These observational conditions reflect the intensity of the underlying thunderstorm system and provide essential practical support for the monitoring and retrieval of hail-related processes [8]. Consequently, to ensure the timeliness of hail prevention and disaster mitigation, higher demands are imposed on the spatiotemporal accuracy of hail early warning systems [9,10].

Currently, hail observation and prediction primarily rely on synoptic scale analysis methods, with a focus on the formation and evolution of hailstorms [11]. S-band polarimetric radar is widely used for hail detection by identifying distinct hailstorm echo characteristics (e.g., high reflectivity factor), while key parameters including the differential reflectivity, specific differential phase, and correlation coefficient are employed to analyze cloud evolution and precipitation processes [12–14]. Alternatively, laser disdrometers are used to record the size and velocity distribution of precipitation particles [15]. However, during hail events, melting during descent often leads to liquid water adhering to hail surfaces, and some hail even melt completely. This results in a complex mixture of raindrops and hail particles in precipitation particles, which increases the difficulty of hail observation [16].

Lidar is an advanced atmospheric remote sensing instrument characterized by a high precision and high spatiotemporal resolution, which exhibits outstanding performance in the field of atmospheric detection [17–19]. Among various lidar systems, coherent Doppler lidar (CDL) has been widely applied in atmospheric detection, with capabilities to detect precipitation [20], melting layers [21,22], gravity waves [23], atmospheric boundary layers [24], wind shear [25], turbulence [26], lightning [5], and aircraft wake vortices [27].

To address the limitations of conventional observations in identifying hail particles and capturing their fine-scale evolution, this study extends the application of CDL to hail observation. Based on the characteristic parameters derived from the CDL power spectrum, a method is developed to effectively identify small hail particles and discriminate hail events. The proposed method enables high-spatiotemporal-resolution observations of hail initiation and evolution, thereby supporting more timely and reliable short-term hail forecasting. Accordingly, the use of CDL shows considerable promise for operational hail early warning and can serve as a promising new tool for high-resolution hail detection.

2. Materials and Methods

2.1. Instruments and Data

This study mainly employed two types of ground-based remote sensing instruments: CDL and OTT Parsivel^2 laser disdrometer (OTT HydroMet GmbH, Kempten, Germany), together with data products from the Fengyun-4A (FY4A) satellite and the ERA5 reanalysis dataset. ERA5 is the fifth-generation global climate reanalysis dataset of the European Centre for Medium Range Weather Forecasts (ECMWF) [28]. In this study, we utilized the ERA5 dataset, including u-v-w wind vectors, temperature, and relative humidity,

with a spatial resolution of 0.25° × 0.25° and a temporal resolution of 1 h. The FY4A is China's new-generation geostationary meteorological satellite [29], and its cloud-type (CLT) product was employed for this study. Both ERA5 and FY4A datasets were applied to analyze the meteorological conditions on the study day.

Specifically, a compact all-fiber CDL system was deployed on the campus of the University of Science and Technology of China (USTC), located at 31.83°N, 117.25°E. Operating at an eye-safe wavelength of 1.5 μm, this CDL system featured a pulse energy of 300 μJ, a repetition rate of 10 kHz, and a maximum detection range of 15 km. For the precipitation experiment reported herein, a vertical observation mode was adopted to enable high-spatiotemporal-resolution measurements of particle vertical velocities. The key parameters are listed in Table 1. Detailed information regarding the validation and application of this CDL system can be found in our previous research [30,31].

Table 1. Key parameters of CDL.

Parameter	Value
Wavelength	1.5 μm
Transmitter type	Pulsed (600 ns)
Transmitter power	3 W
Pulse repetition rate	10 kHz
Time resolution	1 s
Range resolution	30 m
Azimuth scanning range (°)	0–360
Zenith scanning range (°)	0–90

A Parsivel^2 laser disdrometer [32] and a Davis weather station were deployed within a 10 m radius of the CDL system to acquire surface meteorological parameters including precipitation, visibility, temperature, and humidity. The Parsivel^2 captures both the size and speed of surface precipitation particles based on the attenuation of laser beams caused by particle occlusion.

2.2. Methods

Different hydrometeor and aerosol particles exhibit distinct motion velocities, which induce Doppler power spectrum broadening of the backscattered signals detected by the CDL. Under precipitation conditions, the received signal is dominated by scattering contributions from both aerosol particles and precipitation particles [5]. Given that the vertical terminal velocities of precipitation particles are considerably higher than those of aerosol particles, these two particle types typically manifest as two distinct peaks in the Doppler power spectrum.

The Doppler spectrum characteristics of precipitation particles exhibit different patterns under varying precipitation conditions. For raindrops, Doppler spectrum broadening arises from the variability in their particle sizes and fall velocities. Although raindrops of different sizes may exhibit a comparable spectrum width, their Doppler frequency shifts differ owing to discrepancies in fall velocities. The superposition of these individual signals further broadens the Doppler spectrum width [33]. In contrast, the spectrum characteristics of hail particles are far more complex. Previous observational studies have shown that hail has more intricate geometric shapes and size distributions than raindrops, often appearing as spherical or irregular particles with diameters exceeding 5 mm [34,35]. Additionally, hail particles may undergo partial or complete melting during descent as a result of air friction and ambient temperature effects, leading to volume reduction or even complete transformation into liquid raindrops. Therefore, the mixed phase of hail particles and raindrops must be considered when analyzing hail spectrum characteristics. Under these

circumstances, the simultaneous presence of aerosols, hail, and liquid raindrops, which exhibit disparate motion velocities, may result in a tri-modal profile in the Doppler power spectrum., which necessitates analysis using a three-peak Gaussian fitting method. The corresponding mathematical expression is provided below:

$$I(f) = I_a \exp\left[-\frac{(f-f_a)^2}{2\sigma_a^2}\right] + I_r \exp\left[-\frac{(f-f_r)^2}{2\sigma_r^2}\right] + I_h \exp\left[-\frac{(f-f_h)^2}{2\sigma_h^2}\right], \quad (1)$$

where f_a, f_r and f_h represent the Doppler frequency shifts in aerosols, raindrops and hail particles, respectively. I_a, I_r and I_h denote their respective intensity peaks; and σ_a, σ_r and σ_h stand for their respective spectrum widths. The above parameters are determined using the least squares method.

The line-of-sight (LOS) velocity of raindrops or hail particles can be derived from the Doppler frequency shift, following the relationship

$$v_{\mathrm{LOS}} = \frac{\lambda}{2} f_i \quad (2)$$

where f_i is the Doppler frequency shift in different particles, and λ is the laser wavelength of the CDL. Here, the velocity is defined as positive when the particle moves toward the lidar. Using this relationship, the fall velocities of raindrops or hail particles can be retrieved from echo signals at different altitudes.

To further characterize the power spectrum, we introduce the normalized skewness to quantify the symmetry of the frequency spectrum, which is defined as

$$sk = \frac{\sum (v_i - \overline{v})^3 P_i}{\sum P_i} \Big/ \left[\frac{\sum (v_i - \overline{v})^2 P_i}{\sum P_i}\right]^{3/2} - sk_0, \quad (3)$$

where v_i and P_i denote the velocity and power value at the i-th sampling point, respectively, while $\overline{v}$ represents the mean velocity of the power spectrum. sk_0 is the baseline skewness derived from clear-air spectral measurements under conditions of weak turbulence and minimal windshear, where the power spectrum exhibits a unimodal distribution dominated by atmospheric molecular scattering.

Under precipitation conditions, the scattering signals from precipitation particles form additional intensity peaks in the power spectrum, causing the frequency spectrum to deviate from a unimodal distribution. However, the normalized skewness fails to identify such multimodal distributions. For example, when the spectrum contains two peaks of similar intensity, the skewness approaches 0. To accommodate this complex scenario, Equation (3) is revised by redefining $\overline{v}$ as the velocity corresponding to the maximum signal intensity in the spectrum.

In CDL measurements, the quality of raw observational data is commonly evaluated using the carrier-to-noise ratio (CNR), which can be calculated conveniently from the power spectrum in each range bin. For hail detection, a CNR threshold of -27 dB was applied to eliminate low-quality signals and outliers from the dataset. Furthermore, the absolute value of skewness greater than 0.2 was used as an additional constraint to identify hail-related signals, taking advantage of the distinct spectral asymmetry induced by large and irregular hail particles. This combined preprocessing procedure effectively improves data reliability for subsequent hail event identification and analysis.

3. Results

This study is based on observational records obtained on 10 September 2020, during which a hail event was observed over USTC at approximately 21:00 local time (LT). Partial

synchronized data from the Parsivel^2 are listed in Table 2, with a Surface Synoptic Observation (SYNOP) code of 89 recorded at 21:11:30. As defined by the World Meteorological Organization, SYNOP code 89 signifies surface hail, which may occur with or without concurrent rainfall [36].

Table 2. Parsivel^2 data.

Local Time	Rain Rate (mm/h)	Code SYNOP		Particle Number in 10 s
		Value	WMO Code Definition	
10:32:40	2.23	61	Rain, not freezing, continuous (slight)	25
21:11:30	18.28	89	Shower of hail, with or without rain (slight)	59
21:22:30	12.41	63	Rain, not freezing, continuous (moderate)	161

3.1. Hail Event Observations

The formation process of the hail event, monitored by the CDL and other ground-based instruments at USTC, is illustrated in Figure 1. The magenta rectangle contains the hail event. Figure 1a,d show the CNR, spectrum width, spectrum skewness, and vertical velocity measured by the CDL, Figure 1e shows the temperature (blue line) and relative humidity (orange line) from a Vaisala sensor, and Figure 1f shows the visibility (blue line) from the Davis weather station and rainfall rate (orange line) from the Parsivel^2.

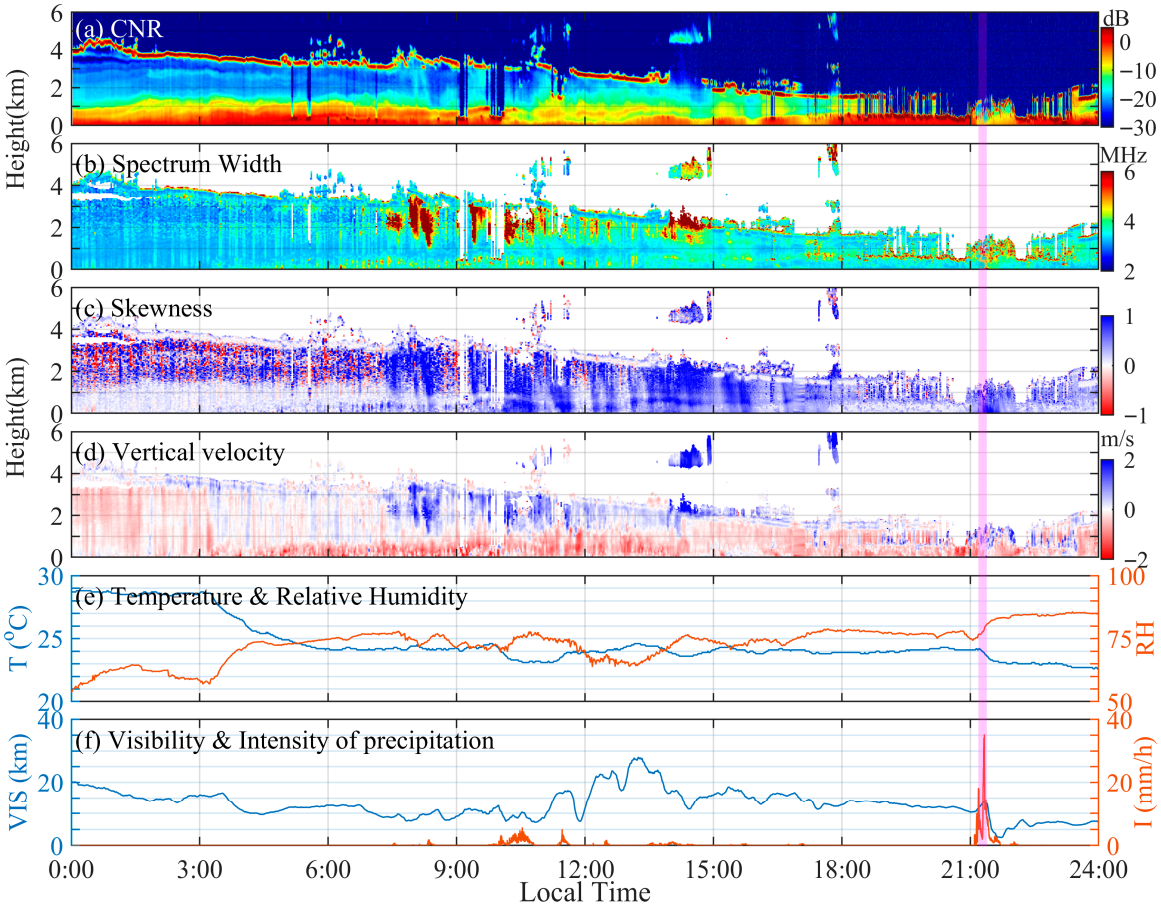

Figure 1. Continuous observation results on 10 September, 2020. (**a**) CNR, (**b**) spectrum width, (**c**) skewness and (**d**) vertical velocity from a CDL. (**e**) Temperature (blue line) and relative humidity (orange line) results from Vaisala; (**f**) visibility (blue line) from Davis weather station and intensity of precipitation (orange line) from Parsivel^2. The magenta rectangle contains hail event.

When no precipitation occurs, the CNR corresponding to aerosols within the altitude range below 1 km approximates 0 dB (Figure 1a). In contrast, during precipitation periods, aerosols are captured by precipitation particles and are subsequently deposited onto the ground, which results in a marked reduction in the aerosol CNR below 1 km. The air mass with a CNR greater than 0 dB above 1 km corresponds to the precipitation cloud base. Since lidar beams are unable to penetrate the convective regions within clouds dominated by large hydrometeors, the precipitation clouds detected by the CDL appear as a thin cloud layer. During the entire precipitation event, precipitation particle populations featuring vertical velocities > 1 m/s beneath the cloud base showed pronounced spectrum broadening and increased skewness; these phenomena are direct evidence of the coexistence of precipitation particles with heterogeneous sizes and velocity magnitudes in the lower cloud layer.

The magenta rectangular area denotes the period during which the hail event occurred (Figure 1). During this interval, the precipitation intensity surged to more than 35 mm/h in a short time. Meanwhile, surface temperature dropped by 1 °C, relative humidity increased by 10%, and atmospheric visibility decreased drastically from 15 km to under 5 km.

3.2. Meteorological Conditions

To further investigate the hail formation process, ERA5 reanalysis data were employed to characterize the synoptic conditions on the day of the event. Figure 2 shows the horizontal wind fields at the 850 hPa, 700 hPa, and 500 hPa pressure levels derived from ERA5 reanalysis data, while Figure 3 displays the vertical cross-sections of wind fields and relative humidity at 117.25°E (the longitude of the USTC).

The 3 h window from 19:00 to 22:00 LT encompasses the pre-hail stage, capturing the development of the hail cloud. As illustrated in Figure 2(a1–a4), the 850 hPa wind field showed a weakly cyclonic pattern around USTC, with winds veering counter-clockwise but lacking a closed vortex. Wind speed maxima were distributed in discrete bands to the northeast and southwest of USTC, with low spatial gradients. These features confirm that the 850 hPa layer acted as the primary convergence zone, driving the upward motion to initiate convection. Due to strong surface friction, rotational characteristics were suppressed, and the layer's main role was to supply moisture and instability energy to the developing convective system.

As illustrated in Figure 2(b1–b4), the 700 hPa wind field displayed a well-defined cyclonic circulation pattern, marked by obvious counter-clockwise wind rotation around USTC. Streamlines showed a strong curvature, providing a clear precursor to a closed vortex structure. Wind speed maxima clustered over the southeast of USTC, forming a distinct high-speed belt with steep spatial gradients—a distribution that was spatially consistent with the location of severe convection. These features demonstrate that the 700 hPa layer dominated by rotational ascending motion represented the mature stage of the convective system. Reduced surface friction at this altitude allowed the cyclonic circulation to couple efficiently with the vertical uplift, forming the critical dynamic framework that maintained hail and other severe convective processes.

As illustrated in Figure 2(c1–c4), the 500 hPa wind field was characterized by prevailing zonal (east–west) uniform flow, with negligible rotational characteristics and a dominant westerly to southwesterly wind direction. In sharp contrast to the cyclonic patterns in the lower (850 hPa) and middle (700 hPa) layers, no cyclonic bending was detected at this altitude. The wind speed field displayed a homogeneous distribution with a substantial magnitude, indicative of the upper-tropospheric jet stream. Functioning as the steering layer for the convective system, the 500 hPa flow contributed to intensifying low-level convergent uplift through the jet-induced suction effect.

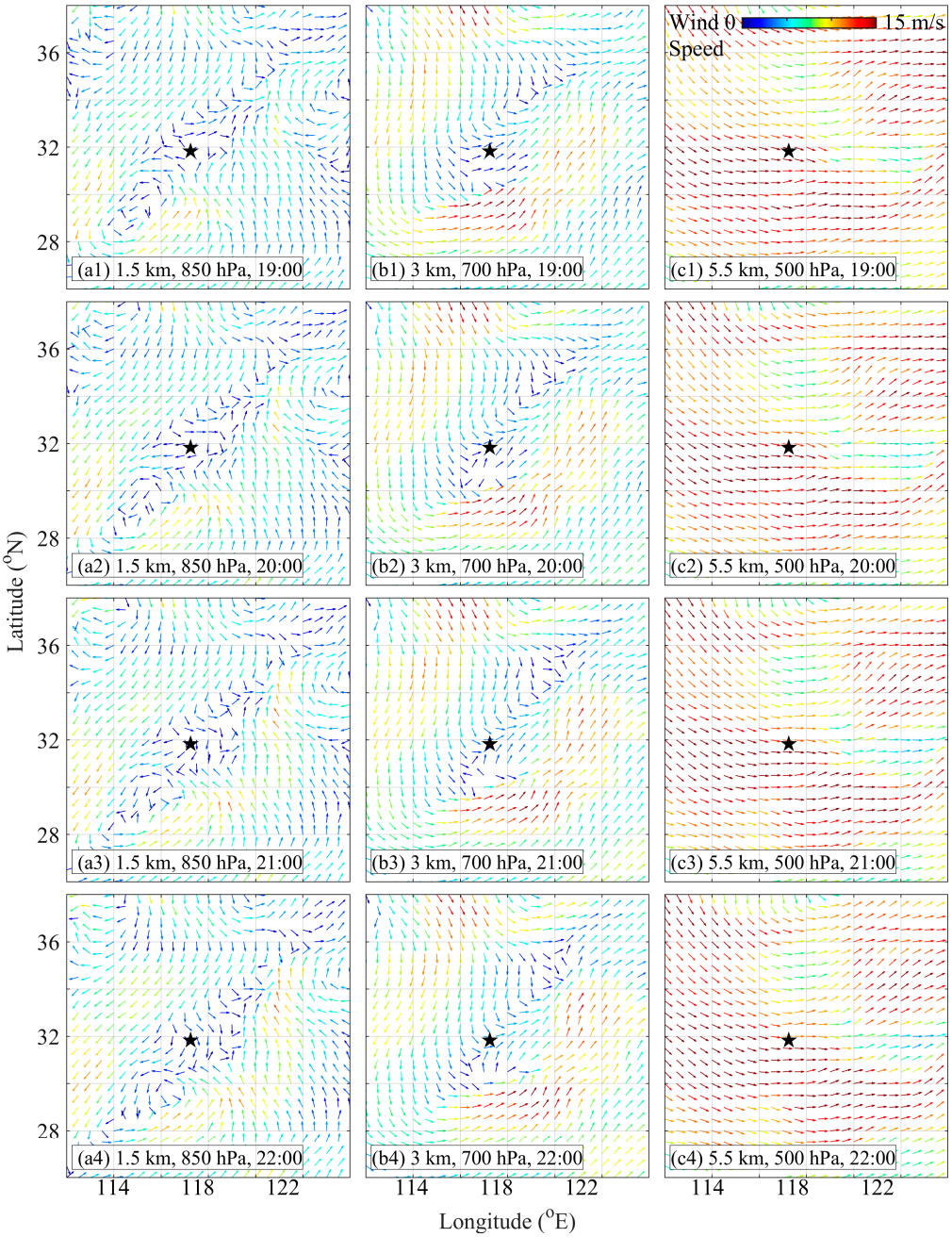

Figure 2. Horizontal wind field at four key instants before, during and after the hail event based on ERA5 reanalysis data. The black pentagram represents the location of USTC.

Figure 3 displays the vertical profiles of wind fields and relative humidity at 117.25°E (USTC longitude), with data sampled at 19:00, 20:00, 21:00, and 22:00 LT. Beneath 700 hPa, a continuous high-humidity region persisted from 19:00 to 22:00 LT, where the wind field exhibited a weak upward convergent motion. As a dedicated moisture source for the convective system, this layer furnished the essential water vapor required to fuel severe convection. In the middle-upper troposphere (above 700 hPa), a distinct dry, warm lid existed between 300 hPa and 400 hPa. This lid suppressed the upward movement of warm and moist air from the lower troposphere, indicating that hail clouds are mainly concentrated at altitudes above 600 hPa.

Figure 4 shows the FY-4A satellite cloud classification product from 20:45 to 21:30 LT. It can be observed that the area over USTC was located at the boundary between liquid water clouds and supercooled water clouds at this time, which provided sufficient moisture

conditions for the formation and growth of hail. Hail particles are primarily formed by accreting supercooled liquid cloud droplets and raindrops within the updrafts of convective clouds. Under rapid growth conditions, the collection of supercooled liquid water by hail releases latent heat during freezing, which may warm the hail surface to 0 °C and maintain a thin layer of liquid water on its surface [37].

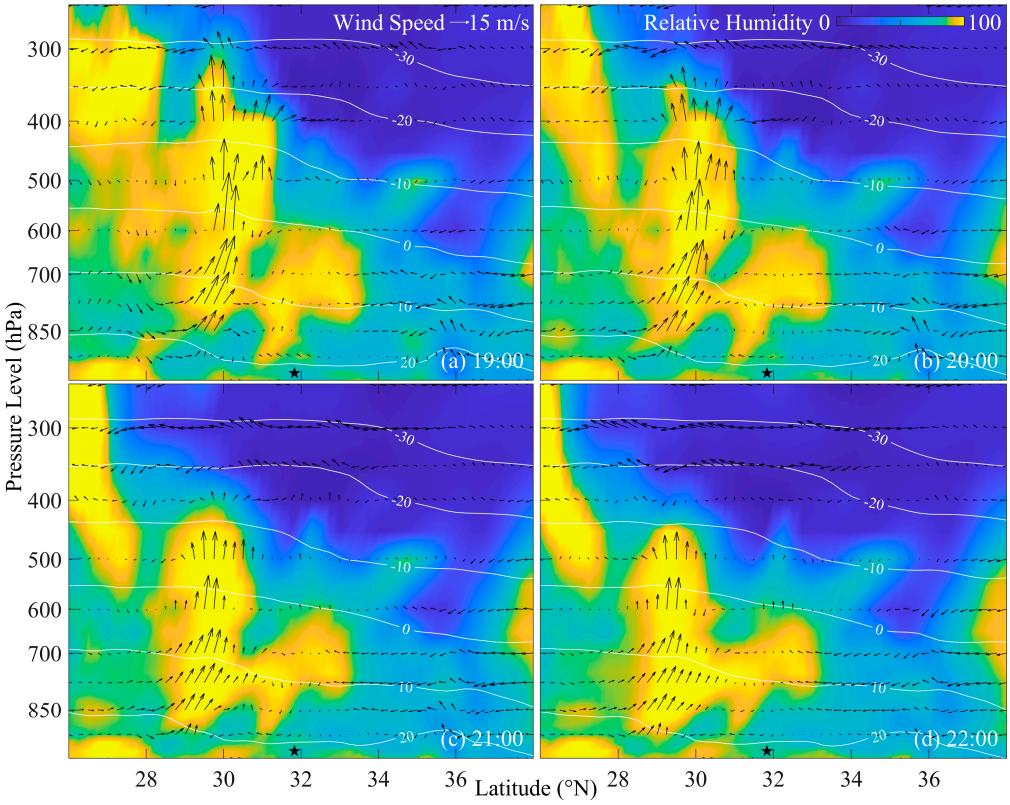

Figure 3. The distribution of ERA5 data of wind vector and relative humidity in the vertical profile of USTC longitude at four key instants before, during and after the hail event. The black pentagram on the ground represents the location of USTC. The white curve represents isotherm ranging from −30 to 20 °C.

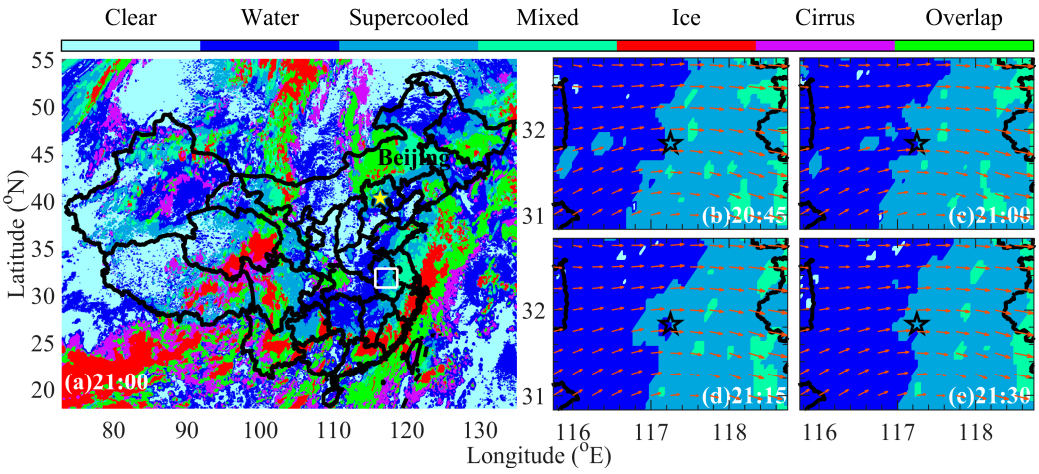

Figure 4. CLT product of FY-4A satellite from 20:45 to 21:30 LT on 10 September 2020. The black pentagram represents the location of USTC. (**a**) shows CLT product across the China region at 21:00 LT; the white square indicates the precipitation region. (**b**–**e**) show CLT product distribution of the hail event at different times. The black pentagram represents the location of USTC. The orange arrows represent the wind vector.

However, spatially continuous satellite imagery indicates no prominent deep convective clouds at high altitudes over the Hefei region, despite abundant atmospheric moisture and the observed occurrence of surface hail. As illustrated in Figure 3, the atmospheric column exhibits a typical structure of warm and moist air in the lower troposphere overlain by dry and cold air intrusions in the middle troposphere, resulting in a distinct upper–dry and lower–moist vertical stratification. Such a configuration is conducive to the development of shallow convection rather than vigorous deep convection [38]. Sufficient supercooled water droplets are concentrated within the temperature layer from −10 °C to 0 °C, allowing graupel particles to grow into small hailstones through repeated collision and coalescence with supercooled water under relatively weak updrafts [39]. Due to the limited intensity of updrafts, hailstones fall to the ground rapidly, while cloud tops fail to develop upward to the −30 °C level where ice crystals are abundant, thus leaving no obvious signature of ice-dominant deep convective clouds in satellite observations.

3.3. Further Discussion

To further confirm the hydrometeor types during the actual precipitation process, the particle size and velocity distributions recorded by the Parsivel^2 were analyzed for the pre-hail period and the one-hour window of hail occurrence, as presented in Figure 5. The black line corresponds to the Atlas raindrop size–velocity empirical model [40], and the red line represents the size–velocity parameterization for hail proposed by Heymsfield and Wright [41]. It can be observed that the particles in Figure 5a are generally consistent with the raindrop curve. In contrast, the particle distribution in Figure 5b does not fully conform to the Atlas raindrop size–velocity empirical equation; most particles lie between the raindrop and hail curves.

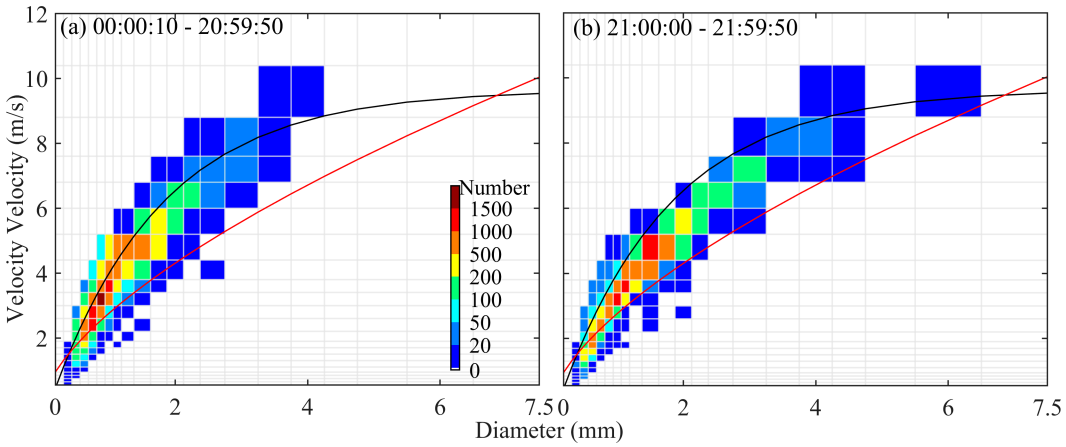

Figure 5. Diameter–velocity distribution of precipitation particles on 10 September 2020: (**a**) 0:00–20:59:50 LT, before hail event; (**b**) 21:00:00–21:59:50 LT, 1 h containing hail event. The black and red curves represent the diameter–velocity relations of raindrops and hail, respectively.

This discrepancy is attributable to the irregular, flattened shape of hail particles: for particles of identical size, flattened hail particles have a lower mass than spherical equivalents, leading to reduced terminal velocities [42]. The mixed presence of such low-velocity hail particles and normal raindrops thus yields the bimodal-like distribution spanning the two curves. Additionally, particles larger than 5 mm account for less than 20 samples, and the particle population is dominated by small-sized hydrometeors. This observation confirms that the surface hail event manifested as a mixed phase of small hail particles and raindrops, which is in good agreement with the conclusions drawn from the meteorological background analysis.

Figure 6 shows the power spectrum detected by the CDL at different altitudes for three typical precipitation events. Each spectrum is normalized to its peak intensity (set to the maximum value), and SW denotes the spectrum width of the raw power spectrum. Specifically, the spectrum at 10:32:39 LT corresponds to light rain (precipitation intensity < 5 mm/h), the spectrum at 21:11:33 LT coincides with the hail occurrence time documented by the Parsivel^2, and the spectrum at 21:22:33 LT represents heavy rain (precipitation intensity > 30 mm/h). Table 3 lists the vertical velocity, spectrum width, and skewness derived from these three cases after removing the aerosol spectrum contribution.

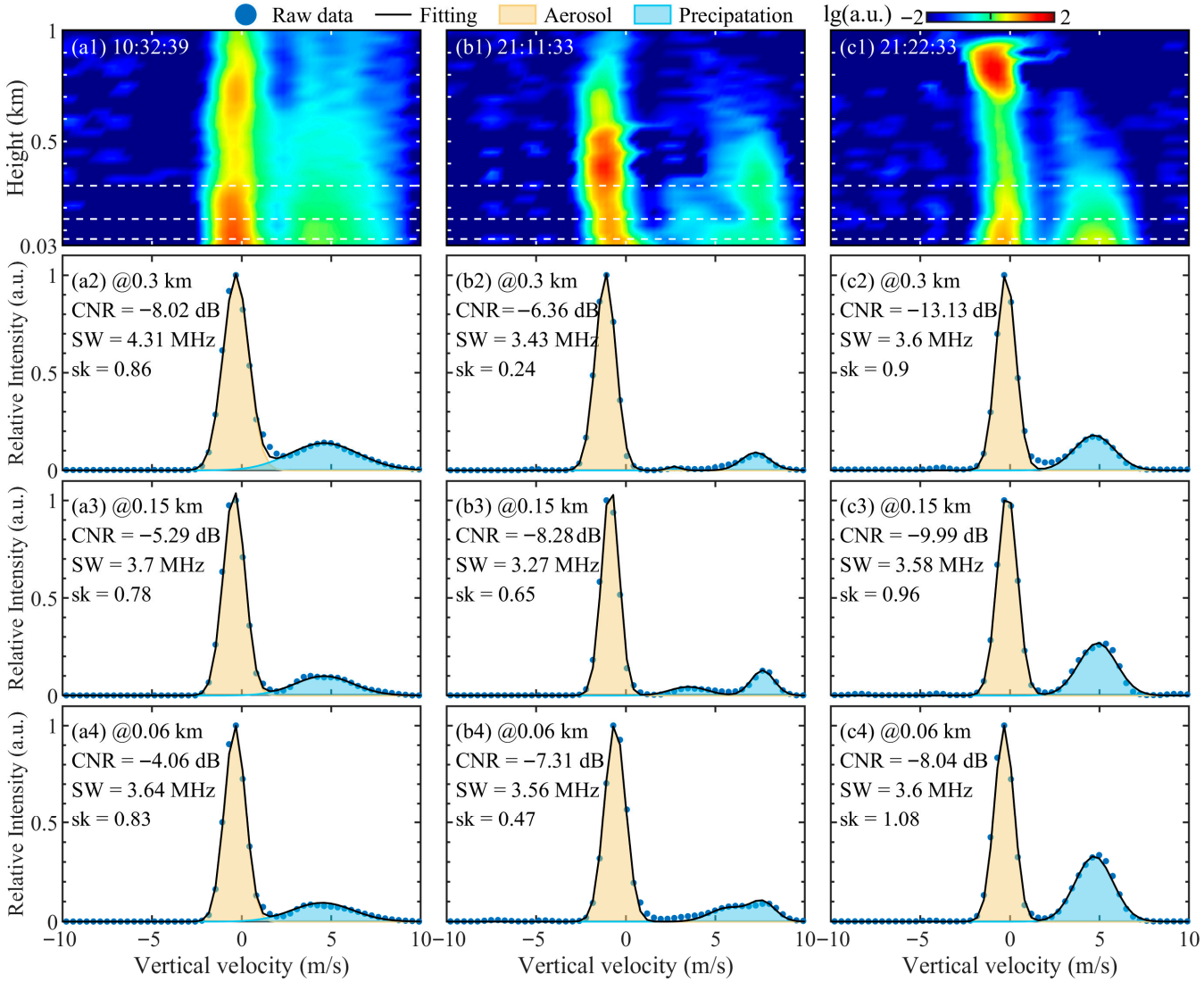

Figure 6. (**a1**–**c1**) are the Doppler power spectrum intensities at different times by CDWL. The three white lines correspond to heights of 0.3 km, 0.15 km, and 0.06 km, respectively. (**a2**–**c4**) are the corresponding detailed Doppler spectra and multi-component Gaussian fitting curves at these three heights. Blue dots represent raw data, the black curves represent the Gaussian fitting, yellow regions represent aerosol signals, and the blue region represents precipitation signals (including raindrops and hail particles).

As can be seen from Figure 6 and Table 3, the power spectrum exhibited a bimodal distribution during both light rain and heavy rain events. After removing the aerosol signal, the velocities derived from the precipitation spectra were consistently below 5 m/s, and the skewness values were close to 0, indicative of symmetric power spectrum profiles.

Table 3. Characteristic parameters of precipitation power spectrum.

Local Time	10:32:39			21:11:33			21:22:33		
Height (km)	0.3	0.15	0.06	0.3	0.15	0.06	0.3	0.15	0.06
Velocity (m/s)	4.64	3.54	3.58	7.44	7.70	6.42	4.41	4.75	4.79
Spectrum width (MHz)	8.69	7.43	8.63	9.12	9.08	10.17	6.70	6.30	5.68
Skewness	−0.09	0.11	0.03	−0.75	−0.99	−0.71	−0.15	0.05	−0.16

Compared with heavy rain, light rain was characterized by a lower signal intensity but broader spectrum width. This discrepancy arises from the fact that small raindrops have weaker inertia and are thus more easily perturbed by environmental turbulence, resulting in an expanded velocity spread and enhanced Doppler broadening without altering the symmetric nature of the precipitation spectrum. On the other hand, the hail event was marked by pronounced increases in velocity, spectrum width, and absolute skewness. These unique power spectrum features stem from the complex microphysical processes of hail particles during descent: under the influence of gravity and temperature, hail particles undergo continuous acceleration, mutual collision, and partial melting, which reduces their particle size and generates a mixture of residual hail fragments and liquid droplets.

A comparison of precipitation spectra between 0.3 km and 0.15 km reveals that the 0.15 km spectrum exhibits a higher vertical velocity, negligible change in spectrum width, and skewness value approaching −1. This trend arises because particles that have fully melted into raindrops fall more slowly, whereas the faster-moving, partially melted hail particles dominate the signal, leading to an increased leftward skew of the spectrum. During further descent to 0.06 km, additional hail particles undergo melting, producing a greater proportion of low-velocity raindrops. This shift in particle composition leads to a reduction in the mean vertical velocity of the spectrum, an expansion of the spectrum width due to the mixed particle velocities, and a decrease in the absolute skewness value as the spectrum becomes more symmetric.

When comparing precipitation spectra from hail and heavy rain events at the same timestamp (21:22:33 LT), several key differences in power spectrum characteristics become apparent. Hail events exhibit higher vertical velocities, exceeding 6 m/s near the surface, contrasting with the sub-5 m/s velocities measured during heavy rain. The spectrum width during hail events exceeds 9 MHz, which is notably larger than that of heavy rain, though comparable to light rain levels. The most striking discrepancy lies in skewness: during hail events, skewness ranges from −0.71 to −0.99, whereas both light and heavy rain events yield near zero skewness values, reflecting the asymmetric nature of hail particle velocity distributions.

To enhance the identification and separation of precipitation and hail signals from Doppler power spectra, we performed a statistical analysis of characteristic parameters across additional precipitation events on the observation day. A dataset of 1595 points was compiled from the 0.03–0.3 km altitude range (0.03 km vertical resolution), including velocity, spectrum width, and skewness, with the results shown in Figure 7.

Velocity was categorized into four bins: 0–2 m/s, 2–4 m/s, 4–7 m/s, and >7 m/s. Points with extremely low skewness in the 0–2 m/s bin are likely artifacts from noise, where aerosol-dominated spectra were incorrectly identified as precipitation. Given that aerosol vertical velocities under convective conditions rarely exceed 2 m/s [43], only velocities >2 m/s are treated as valid precipitation signals.

Notably, spectrum width shows a significant variability near 3 m/s. Based on Atlas, Srivastava and Sekhon [40], a rainfall velocity of about 3 m/s corresponds to a raindrop diameter of about 0.73 mm. These small droplets exhibit weak backscattering and fall at

velocities comparable to aerosols, making it challenging to deconvolve their overlapping Doppler spectra. This leads the bimodal Gaussian fitting to converge to a local optimum, introducing substantial errors that result in either inflated or deflated spectrum width estimates [44].

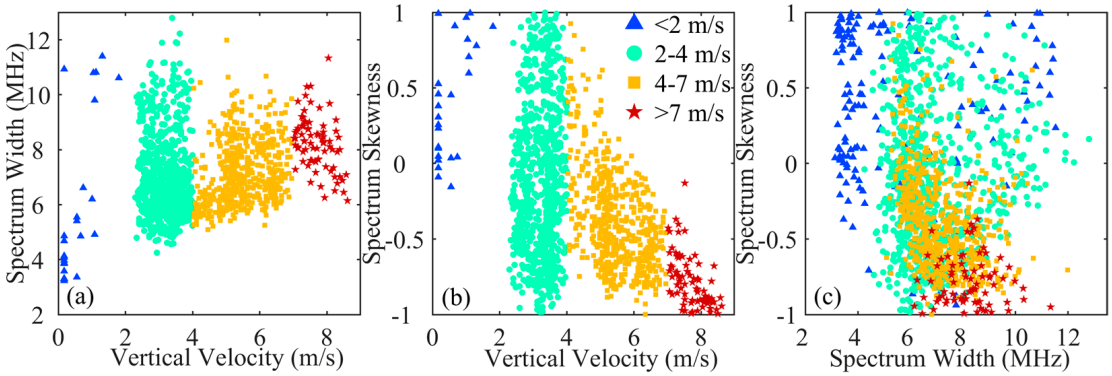

Figure 7. Statistical results of precipitation data from that very day. (**a**) shows the scatter plots of spectrum width versus velocity. (**b**) shows the scatter plots of skewness versus velocity. (**c**) shows the scatter plots of skewness versus spectrum width. The blue triangles, light-green circles, yellow squares, and red pentagrams represent data points with velocities less than 2 m/s, between 2 and 4 m/s, between 4 and 7 m/s, and greater than 7 m/s, respectively.

In the 4–7 m/s range, spectrum width is more clustered, with most absolute skewness values below 0.5. In contrast, points with velocities > 7 m/s predominantly show a spectrum width > 7 MHz, while those in the 4–7 m/s range mostly lie between 5 and 7 MHz, with absolute skewness values approaching 1. The hail events produce multimodal power spectra due to the partial melting of hail particles (Figure 6), but this analysis relied exclusively on bimodal Gaussian fitting for all data. This discrepancy may account for the occurrence of data points with anomalously low spectrum width or near zero skewness.

4. Conclusions

Hail events are characterized by rapid onset, posing substantial challenges to short-term nowcasting operations. To address this critical issue, this study presents an in-depth analysis of CDL power spectra collected during a hail event that occurred on 10 September 2020 in Hefei. A Gaussian fitting method was employed to eliminate aerosol signal interference, thereby isolating valid precipitation signals for subsequent analysis. Comparative assessments were conducted across three distinct precipitation scenarios, light rain, heavy rain, and hail, with statistical analyses used to delineate the unique power spectrum characteristics of hail events.

The statistical results presented above clearly demonstrate that hail and rainfall yield distinguishable characteristics in CDL power spectra. Specifically, precipitation signals associated with hail are characterized by higher vertical velocities; moreover, within the high-velocity signal category, hail containing precipitation is further differentiated by wider spectrum widths and absolute skewness values close to 1. Notably, the hail event in this study formed under weak convective conditions, resulting in the co-occurrence of hail particles and raindrops. Even under this mixed-phase precipitation scenario, the CDL power spectrum enabled the identification of periods dominated by hail particles. Leveraging the superior spatiotemporal resolution of lidar systems, this power spectrum discrimination method holds the potential for delivering high-precision observational data to support the nowcasting of hail events.

In future work, we will analyze hail events in different regions and seasons to accumulate hail samples. Using size, velocity, and CDL power spectrum parameters, we will further develop and iteratively optimize the CDL hail identification algorithm. We will also attempt to enhance the cloud penetration capability of the system by increasing laser power, which will facilitate the investigation of particle velocity variations within hail clouds and support the development of early warning systems for hail precipitation. We also plan to integrate polarization detection into the lidar system to enable more detailed observations of particle phase transitions in hail clouds.

Author Contributions: Conceptualization, K.W.; methodology, K.W.; software, K.W. and J.H.; validation, K.W. and Y.S.; formal analysis, K.W., Y.S. and T.W.; investigation, K.W.; resources, X.H. and H.X.; data curation, K.W.; writing—original draft preparation, K.W.; writing—review and editing, K.W., Y.S., J.H., T.W., M.W. and H.X.; visualization, K.W.; supervision, H.X.; funding acquisition, K.W. All authors have read and agreed to the published version of the manuscript.

Funding: This research was funded by the Research Project of Huangshan University (grant number 2025xkjq001).

Data Availability Statement: The data presented in this study are available on request from the corresponding author.

Conflicts of Interest: The authors declare no conflicts of interest.

References

1. Kahraman, A.; Kendon, E.J.; Fowler, H.J.; Short, C.J. Future changes in severe hail across Europe, including regional emergence of warm-type thunderstorms. *Nat. Commun.* **2025**, *16*, 8438. [CrossRef] [PubMed]
2. Battaglioli, F.; Taszarek, M.; Groenemeijer, P.; Púčik, T.; Rädler, A. Contrasting trends in very large hail events and related economic losses across the globe. *Nat. Geosci.* **2026**, *19*, 52–58. [CrossRef]
3. Mahoney, K.; Alexander, M.A.; Thompson, G.; Barsugli, J.J.; Scott, J.D. Changes in hail and flood risk in high-resolution simulations over Colorado's mountains. *Nat. Clim. Change* **2012**, *2*, 125–131. [CrossRef]
4. Fan, J.; Rosenfeld, D.; Zhang, Y.; Giangrande, S.E.; Li, Z.; Machado, L.A.T.; Martin, S.T.; Yang, Y.; Wang, J.; Artaxo, P.; et al. Substantial convection and precipitation enhancements by ultrafine aerosol particles. *Science* **2018**, *359*, 411–418. [CrossRef]
5. Wu, K.; Wei, T.; Yuan, J.; Xia, H.; Huang, X.; Lu, G.; Zhang, Y.; Liu, F.; Zhu, B.; Ding, W. Thundercloud structures detected and analyzed based on coherent Doppler wind lidar. *Atmos. Meas. Tech.* **2023**, *16*, 5811–5825. [CrossRef]
6. Kumjian, M.R.; Lombardo, K.; Loeffler, S. The Evolution of Hail Production in Simulated Supercell Storms. *J. Atmos. Sci.* **2021**, *78*, 3417–3440. [CrossRef]
7. Kumjian, M.R.; Lombardo, K. A Hail Growth Trajectory Model for Exploring the Environmental Controls on Hail Size: Model Physics and Idealized Tests. *J. Atmos. Sci.* **2020**, *77*, 2765–2791. [CrossRef]
8. Katona, B.; Markowski, P. Assessing the Influence of Complex Terrain on Severe Convective Environments in Northeastern Alabama. *Weather Forecast.* **2021**, *36*, 1003–1029. [CrossRef]
9. Wu, Q.; Shou, Y.-X.; Zheng, Y.-G.; Wu, F.; Wang, C.-Y. Detecting Hailstorms in China from FY-4A Satellite with an Ensemble Machine Learning Model. *Remote Sens.* **2024**, *16*, 3354. [CrossRef]
10. Fuchs, B.R.; Rutledge, S.A.; Bruning, E.C.; Pierce, J.R.; Kodros, J.K.; Lang, T.J.; MacGorman, D.R.; Krehbiel, P.R.; Rison, W. Environmental controls on storm intensity and charge structure in multiple regions of the continental United States. *J. Geophys. Res. Atmos.* **2015**, *120*, 6575–6596. [CrossRef]
11. Soula, S.; Seity, Y.; Feral, L.; Sauvageot, H. Cloud-to-ground lightning activity in hail-bearing storms. *J. Geophys. Res. Atmos.* **2004**, *109*, D02101. [CrossRef]
12. Jiang, S.; Lyu, F.; Cummer, S.A.; Zheng, T.; Wang, M.; Liu, Y.; Lyu, W. A Case Study on the Vertical Distribution and Correlation Between Low-Frequency Lightning Sources and Hydrometeors During a Thunderstorm. *Remote Sens.* **2025**, *17*, 2676. [CrossRef]
13. Luo, L.; Xue, M.; Zhu, K.; Zhou, B. Explicit prediction of hail using multimoment microphysics schemes for a hailstorm of 19 March 2014 in eastern China. *J. Geophys. Res. Atmos.* **2017**, *122*, 7560–7581. [CrossRef]
14. Takahashi, N.; Kosaka, T. Evaluation of the flagGraupelHail Product from Dual-Frequency Precipitation Radar Onboard the Global Precipitation Measurement Core Observatory Using Multi-Parameter Phased Array Weather Radar. *Remote Sens.* **2025**, *17*, 3741. [CrossRef]

15. Chen, P.; Wang, P.; Li, Z.; Yang, Y.; Jia, Y.; Yang, M.; Peng, J.; Li, H. Raindrop Size Distribution Characteristics of Heavy Precipitation Events Based on a PWS100 Disdrometer in the Alpine Mountains, Eastern Tianshan, China. *Remote Sens.* **2023**, *15*, 5068. [CrossRef]
16. Dai, Y.; Wang, W.; Xu, Y.; Li, Y.; Liu, T. Experimental study on the influence of turbulence on hail impacts. *Sci. Rep.* **2024**, *14*, 18317. [CrossRef]
17. Wei, T.; Wang, M.; Jiang, P.; Wu, K.; Zhang, Z.; Yuan, J.; Xia, H.; Lolli, S. Retrieving aerosol backscatter coefficient using coherent Doppler wind lidar. *Opt. Express* **2025**, *33*, 6832–6849. [CrossRef]
18. Liu, J.; Yuan, J.; Yang, H.; Chen, A.; Gu, Y.; Wei, T.; Xia, H. Research on impact of range resolutions on wind detection performance using virtual lidar. *Opt. Express* **2025**, *33*, 32386–32397. [CrossRef]
19. Yuan, J.; Wu, Y.; Shu, Z.; Su, L.; Tang, D.; Yang, Y.; Dong, J.; Yu, S.; Zhang, Z.; Xia, H. Real-Time Synchronous 3-D Detection of Air Pollution and Wind Using a Solo Coherent Doppler Wind Lidar. *Remote Sens.* **2022**, *14*, 2809. [CrossRef]
20. Wei, T.; Xia, H.; Yue, B.; Wu, Y.; Liu, Q. Remote sensing of raindrop size distribution using the coherent Doppler lidar. *Opt. Express* **2021**, *29*, 17246–17257. [CrossRef] [PubMed]
21. Yuan, J.; Wu, K.; Wei, T.; Wang, L.; Shu, Z.; Yang, Y.; Xia, H. Cloud Seeding Evidenced by Coherent Doppler Wind Lidar. *Remote Sens.* **2021**, *13*, 3815. [CrossRef]
22. Wei, T.; Xia, H.; Wu, K.; Yang, Y.; Liu, Q.; Ding, W. Dark/bright band of a melting layer detected by coherent Doppler lidar and micro rain radar. *Opt. Express* **2022**, *30*, 3654–3664. [CrossRef] [PubMed]
23. Jia, M.; Yuan, J.; Wang, C.; Xia, H.; Wu, Y.; Zhao, L.; Wei, T.; Wu, J.; Wang, L.; Gu, S.Y.; et al. Long-lived high-frequency gravity waves in the atmospheric boundary layer: Observations and simulations. *Atmos. Chem. Phys.* **2019**, *19*, 15431–15446. [CrossRef]
24. Smalikho, I.N.; Banakh, V.A. Measurements of wind turbulence parameters by a conically scanning coherent Doppler lidar in the atmospheric boundary layer. *Atmos. Meas. Tech.* **2017**, *10*, 4191–4208. [CrossRef]
25. Xia, H.; Chen, Y.; Yuan, J.; Su, L.; Yuan, Z.; Huang, S.; Zhao, D. Windshear Detection in Rain Using a 30 km Radius Coherent Doppler Wind Lidar at Mega Airport in Plateau. *Remote Sens.* **2024**, *16*, 924. [CrossRef]
26. Wang, L.; Yuan, J.; Xia, H.; Zhao, L.; Wu, Y. Marine Mixed Layer Height Detection Using Ship-Borne Coherent Doppler Wind Lidar Based on Constant Turbulence Threshold. *Remote Sens.* **2022**, *14*, 745. [CrossRef]
27. Yuan, J.; Su, L.; Xia, H.; Li, Y.; Zhang, M.; Zhen, G.; Li, J. Microburst, Windshear, Gust Front, and Vortex Detection in Mega Airport Using a Single Coherent Doppler Wind Lidar. *Remote Sens.* **2022**, *14*, 1626. [CrossRef]
28. Hersbach, H.; Bell, B.; Berrisford, P.; Hirahara, S.; Horányi, A.; Muñoz-Sabater, J.; Nicolas, J.; Peubey, C.; Radu, R.; Schepers, D.; et al. The ERA5 global reanalysis. *Q. J. R. Meteorol. Soc.* **2020**, *146*, 1999–2049. [CrossRef]
29. Yang, J.; Zhang, Z.; Wei, C.; Lu, F.; Guo, Q. Introducing the New Generation of Chinese Geostationary Weather Satellites, Fengyun-4. *Bull. Am. Meteorol. Soc.* **2017**, *98*, 1637–1658. [CrossRef]
30. Yuan, J.; Xia, H.; Wei, T.; Wang, L.; Yue, B.; Wu, Y. Identifying cloud, precipitation, windshear, and turbulence by deep analysis of the power spectrum of coherent Doppler wind lidar. *Opt. Express* **2020**, *28*, 37406–37418. [CrossRef]
31. Wei, T.; Xia, H.; Wu, Y.; Yuan, J.; Wang, C.; Dou, X. Inversion probability enhancement of all-fiber CDWL by noise modeling and robust fitting. *Opt. Express* **2020**, *28*, 29662–29675. [CrossRef]
32. Tokay, A.; Wolff, D.B.; Petersen, W.A. Evaluation of the New Version of the Laser-Optical Disdrometer, OTT Parsivel2. *J. Atmos. Ocean. Technol.* **2014**, *31*, 1276–1288. [CrossRef]
33. Wei, T.; Xia, H.; Hu, J.; Wang, C.; Shangguan, M.; Wang, L.; Jia, M.; Dou, X. Simultaneous wind and rainfall detection by power spectrum analysis using a VAD scanning coherent Doppler lidar. *Opt. Express* **2019**, *27*, 31235–31245. [CrossRef]
34. Chen, Q.; Yin, Y.; Jiang, H.; Chu, Z.; Xue, L.; Shi, R.; Zhang, X.; Chen, J. The Roles of Mineral Dust as Cloud Condensation Nuclei and Ice Nuclei During the Evolution of a Hail Storm. *J. Geophys. Res. Atmos.* **2019**, *124*, 14262–14284. [CrossRef]
35. Jing, Y.; Chen, Y.; Ma, X.; Ma, J.; Li, X.; Ma, N.; Bi, K. Characteristics of Summer Hailstorms Observed by Radar and Himawari-8 in Beijing, China. *Remote Sens.* **2022**, *14*, 5843. [CrossRef]
36. World Meteorological Organization. *Manual on Codes—International Codes, Volume I.1: Part A—Alphanumeric Codes*; World Meteorological Organization: Geneva, Switzerland, 2015. [CrossRef]
37. Allen, J.T.; Giammanco, I.M.; Kumjian, M.R.; Jurgen Punge, H.; Zhang, Q.; Groenemeijer, P.; Kunz, M.; Ortega, K. Understanding Hail in the Earth System. *Rev. Geophys.* **2020**, *58*, e2019RG000665. [CrossRef]
38. Takahashi, N.; Kurosawa, Y. Evaluation of Global Precipitation Measurement (GPM) Dual-Frequency Precipitation Radar (DPR) Heavy Ice Precipitation Products. *J. Atmos. Ocean. Technol.* **2025**, *42*, 1063–1084. [CrossRef]
39. Handler, S.L.; Homeyer, C.R. Radar-Observed Bulk Microphysics of Midlatitude Leading-Line Trailing-Stratiform Mesoscale Convective Systems. *J. Appl. Meteorol. Climatol.* **2018**, *57*, 2231–2248. [CrossRef]
40. Atlas, D.; Srivastava, R.C.; Sekhon, R.S. Doppler radar characteristics of precipitation at vertical incidence. *Rev. Geophys.* **1973**, *11*, 1–35. [CrossRef]
41. Heymsfield, A.; Wright, R. Graupel and Hail Terminal Velocities: Does a "Supercritical" Reynolds Number Apply? *J. Atmos. Sci.* **2014**, *71*, 3392–3403. [CrossRef]

42. Sánchez, J.L.; Gil-Robles, B.; Dessens, J.; Martin, E.; Lopez, L.; Marcos, J.L.; Berthet, C.; Fernández, J.T.; García-Ortega, E. Characterization of hailstone size spectra in hailpad networks in France, Spain, and Argentina. *Atmos. Res.* **2009**, *93*, 641–654. [CrossRef]
43. Dagan, G.; Koren, I.; Altaratz, O. Quantifying the effect of aerosol on vertical velocity and effective terminal velocity in warm convective clouds. *Atmos. Chem. Phys.* **2018**, *18*, 6761–6769. [CrossRef]
44. Niu, S.; Jia, X.; Sang, J.; Liu, X.; Lu, C.; Liu, Y. Distributions of Raindrop Sizes and Fall Velocities in a Semiarid Plateau Climate: Convective Versus Stratiform Rains. *J. Appl. Meteorol. Climatol.* **2010**, *49*, 632–645. [CrossRef]